Magnetic Resonance Imaging 61 (2019) 224–230

Contents lists available at ScienceDirect

Magnetic Resonance Imaging

journal homepage: www.elsevier.com/locate/mri

Original contribution

Analyzing spatially and temporally visualized formation behavior of methane hydrate in unconsolidated porous media

Lunxiang Zhang[a,1], Lingjie Sun[a,1], Mingrui Sun[a], Xin Lv[b], Hongsheng Dong[a], Yang Miao[c], Lei Yang[a], Yongchen Song[a], Jiafei Zhao[a,*]

[a] Key Laboratory of Ocean Energy Utilization and Energy Conservation of Ministry of Education, School of Energy and Power Engineering, Dalian University of Technology, Dalian 116024, China
[b] CNOOC Research Institute, Beijing 100027, China
[c] Xingang Shipbuilding Heavy Industry Co., Ltd., Tianjin 300452, China

ARTICLE INFO

Keywords:
Natural gas hydrate
Formation behavior
Blockage
Migration path
Magnetic resonance imaging

ABSTRACT

An understanding of the nucleation and growth mechanism of methane hydrate in porous space is essential for exploitation and application of hydrates, but the mechanism is yet to be clarified. Magnetic resonance imaging (MRI) was employed to visually analyze the spatial and temporal formation behavior of methane hydrate in a porous media. Detailed information about the water distribution, initial nucleation sites, and hydrate growth was obtained, in addition to MRI images. The results demonstrated that the water molecules distributed in the vertical direction preferred the middle slice of a porous medium sample, and the decrease in the number of molecules in the middle slice and on both sides of the slice was similar during hydrate formation. The formation process are quite different in selected horizontal slices, which were contributed to the various distribution of water and gas in pore spaces and the randomness of methane hydrate formation. The extension of these predicted results could have important implications for optimizing the formation processes of gas hydrate in hydrate-based technologies.

1. Introduction

Natural gas hydrate, also known as methane hydrate ($CH_4{\cdot}5.75H_2O$ or $4CH_4{\cdot}23H_2O$) is an ice-like, non-stoichiometric crystalline compound that develops when small guest molecules are encased in host frameworks of water molecules formed by hydrogen bonding at low temperature and under high pressure [1,2]. Natural gas hydrate widely exists in marine environments and regions with permafrost. It is estimated that the total amount of hydrocarbons contained in existing fossil fuels is only half that in natural gas hydrate [3]. Therefore, the exploitation of natural gas hydrate can help address issues regarding energy shortage and environmental pollution. Moreover, many countries regard natural gas hydrate as an important energy source [4].

Although there are various methods to extract natural gas from its hydrate form, such as thermal stimulation, depressurization, inhibitor injection, and carbon dioxide replacement, the actual execution is still difficult and the technology has yet to be realized in commercial mining applications [5,6]. The nucleation and growth mechanism of gas hydrates in porous space or natural sediments is not well understood, and it remains a great challenge to describe the kinetics of hydrate formation because of the stochastic nucleation and the large number of molecules and long period of time required for the growth process [1]. However, hydrate exploitation depends on the dynamic characteristics of hydrate formation in a porous microstructure because the mechanical strength and permeability of the hydrate-bearing sediments have an important effect on heat and mass transfer [7]. The hydro-thermo-chemo-mechanical coupling process during hydrate formation and dissociation affects the spatial distribution of hydrate molecules in the sediment, which in turn controls gas production during the mining process [8,9]. Moreover, the enhancement of the kinetic conversion of water to hydrate is also the key factor for carbon capture [10] and natural gas separation [11], cool storage [12], heavy-metal separation [13], and other hydrate applications.

Therefore, it is essential to study the formation characteristics of hydrates in porous media. Several methods, such as powder X-ray diffraction (XRD), Raman spectroscopy, X-ray computed tomography (X-

Abbreviations: ^{13}C NMR, carbon-13 nuclear magnetic resonance; ^{1}H MRI, hydrogen-1 magnetic resonance imaging; MI, mean intensity; XRD, X-ray diffraction

* Corresponding author.
E-mail address: jfzhao@dlut.edu.cn (J. Zhao).

[1] These authors contributed equally to this work and should be regarded as co-first authors.

https://doi.org/10.1016/j.mri.2019.06.005
Received 5 May 2019; Received in revised form 28 May 2019; Accepted 2 June 2019

ray CT), and magnetic resonance imaging (MRI), have been used to study hydrate formation and dissociation. Tang et al. obtained the development of diffraction peaks as a function of time during hydrate formation via in situ XRD [14]. Kida et al. studied the effect of guest composition and structural properties on the lattice parameters and density via powder XRD and solid-state carbon-13 nuclear magnetic resonance (^{13}C NMR) spectroscopy [15]. Using Raman spectroscopy, Li et al. examined the hydrate nucleation mechanism in the presence of hydrophobized particles and established a quantitative relationship between hydrate-nucleation promotion and water-molecule ordering near the solid surface [16]. Cheng et al. used the MRI signal intensity to study the growth and dissociation characteristics of CO_2 hydrate in porous media with different pore sizes under different pressures and at different temperatures [17]. Among these methods, MRI has been widely used in material and engineering science, and the entire process of hydrate formation and dissociation can be clearly observed, even in porous media.

As briefly discussed, MRI is an emerging technology applied in porous medium to overcome the deficiently spatial and temporal resolution in traditionally in-situ observation method. For instance, a full-3D-CT scanning of crystal hydrate in porous medium spent over tens of minutes [18]. Furthermore, limited studies have focused on the spatial and temporal characteristic of methane hydrate formation by using MRI, although extensive in-situ observations of methane hydrate dissociation with MRI monitor have been conducted in the past few decades [19–21]. Thus, in this study, the spatial and temporal formation behavior of methane hydrate in unconsolidated porous media was studied with an ^{1}H MRI system. Experiments on methane hydrate formation were carried out in media with different levels of water saturation. The pressure, mean intensity (MI), water saturation (S_w), gas saturation (S_g), hydrate saturation (S_h), and MRI images during the hydrate formation process were obtained and analyzed. Different slices of the sample in the vertical and horizontal directions were selected to analyze the characteristics of water and gas migration during hydrate formation. The findings could provide guidelines for hydrate exploitation, gas storage and separation, cool storage, and other hydrate applications.

2. Experimental section

2.1. Materials

The CH_4 gas (99.99%) used in this study for hydrate formation was supplied by Dalian Special Gas Co. Ltd., Dalian, China. Quartz glass beads (0.18–0.22 mm; mean particle size d = 0.2 mm; specific gravity G_s = 1.5) (BZ-02 ASONE, Co., Ltd., Osaka, Japan) were mixed with deionized water (resistivity ρ = 18.2 MΩ·cm at 25 °C). The MRI experimental temperature was controlled by a coolant (Fluorinert FC-40, 3M, St. Paul, MN, USA), which was a non-magnetic liquid and could not be visualized by MRI, and therefore minimized the interference of radio frequency (RF) field artifacts on the imaging system. Additional details about the materials can be found in our previous works [19–21].

2.2. Experimental apparatus

Fig. 1 shows the apparatus employed in this experiment. It mainly consisted of an MRI system (Varian, Inc., Palo Alto, CA, USA) with a high-pressure MRI chamber, two syringe pumps (260D, Teledyne ISCO Inc., Lincoln, NE, USA), two refrigerated circulators (F25-ME, JULABO INV., Seelbach, Germany), a vacuum pump (SHB-11 A, SJSK Exp. Co., Ltd., Tianjin, China), and a data acquisition system.

The inner diameter and length of the high-pressure MRI chamber (made of non-magnetic materials) were 15 and 200 mm, respectively, and the maximum working pressure was 15 MPa. A cooling jacket was wrapped around the high-pressure MRI chamber to control the temperature within the range of −28 to 200 °C with a precision of ± 0.01 K. Compared with ^{1}H in methane or solids (methane hydrate or ice), ^{1}H in liquid water has a much longer transverse relaxation time. Therefore, only ^{1}H in liquid water could be detected by the experimental MRI system (operating at 400 MHz and 9.4 T) with a spin-echo multi-slice (SEMS) pulse sequence. The parameters of the SEMS used in this study were as follows: time of repetition = 1000 ms; time of echo = 4.39 ms; field of view = 30 mm × 30 mm; thickness = 4.0 mm; image date matrix = 128 pixel × 128 pixel; voxel resolution = 0.234 × 0.234 mm^2/pixel^2; and acquisition time = 128 s. One syringe pump was used to inject water (or gas) into the high-pressure MRI chamber, while the back pressure was maintained by the other syringe pump. The refrigerated circulators were used to provide constant-temperature conditions for the experimental system (including gas, water, and high-pressure MRI chamber). The temperature of the high-pressure MRI chamber was monitored by a thermocouple (Yamari Industries, Osaka, Japan) with a precision of ± 0.1 K in the range of 245–473 K, while the pressure was monitored by two pressure transducers (Nagano Co., Ltd., Shizuoka, Japan) with a precision of ± 0.1 MPa in the range of 0–27.6 MPa. The thermocouple and pressure transducers were connected to the data acquisition system.

2.3. Experimental procedure

First, the BZ-02 quartz glass beads were packed into the high-pressure MRI chamber. Next, the high-pressure MRI chamber was placed into the MRI system and connected to the experimental devices. The air in the high-pressure MRI chamber was evacuated by the vacuum pump for 0.5 h. Deionized water was then injected from the bottom of the high-pressure MRI chamber until the porous medium was fully saturated and remained stable for 1 h. Low-pressure CH_4 gas was injected into the porous medium from the top of the high-pressure MRI chamber. Meanwhile, the deionized water was discharged. Once the targeted water saturation in the porous medium was obtained, the high-pressure MRI chamber was closed and cooled to 275.15 K by the refrigerated circulator. When the temperature of the high-pressure MRI chamber reached 275.15 K, cooled high-pressure CH_4 gas (275.15 K, and 4.2 MPa) was injected into the high-pressure MRI chamber until the target pressure was obtained. During the process of hydrate formation, the intensity of ^{1}H signals was monitored by the MRI system. Additional details about the experimental procedure can be found in our previous works [19–21].

3. Results and discussion

Saturation (S) is defined as the volume of one component (water, methane hydrate, or gas) relative to the total volume of pore space in the porous medium. The mean intensity (MI) of ^{1}H signals in MRI images reflects the liquid water distribution and could be used to calculate the water saturation. When the porous medium was fully saturated with deionized water, the MI was defined as I_{full}. After partial deionized water was discharged by the injected low-pressure CH_4 gas, the MI was described as I_0, thus, the initial water saturation (S_{w0}) could be calculated in Eq. (1):

$$S_{w0} = \frac{I_0}{I_{full}}, \tag{1}$$

With methane hydrate formations, liquid water was consumed and MIs decreased. I_i represents the MI at the ith min and corresponding water saturation could be described using Eq. (2):

$$S_w = \frac{I_i \times S_{w0}}{I_0}, \tag{2}$$

The following Eq. (3) is generally used to describe the reaction of methane hydrate formation and dissociation:

$$CH_4 + h_w H_2O \rightleftharpoons CH_4 \cdot h_w H_2O \tag{3}$$

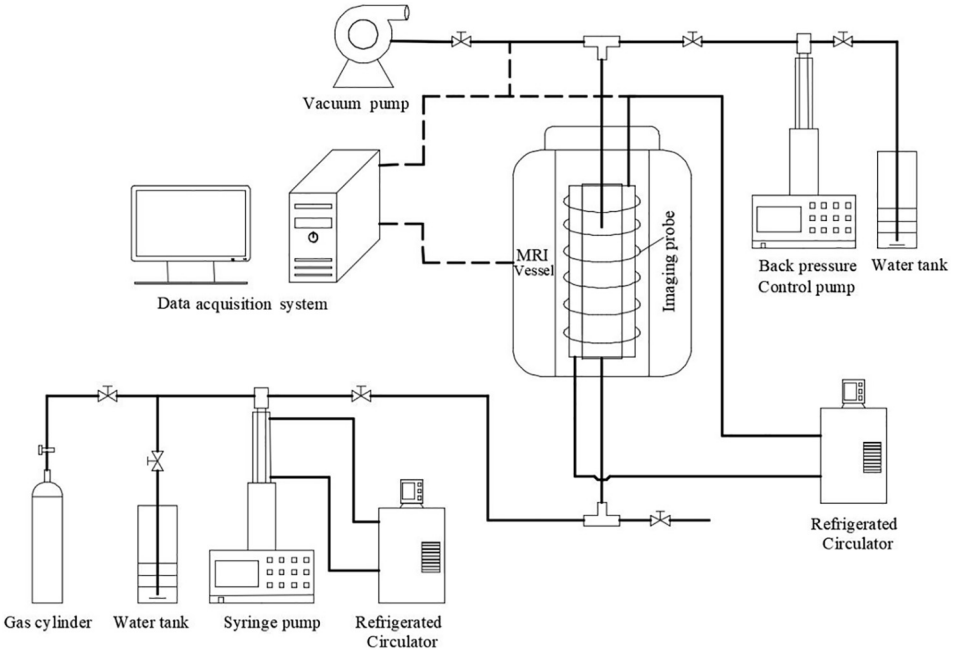

Fig. 1. Schematic diagram of experimental MRI system.

Here, h_w is the molar mass of methane hydrate when the hydrate number is 6 [2].

For forming 1 mol of methane hydrate, the volumes of reacted water and formed hydrate are described in Eqs. (4) and (5):

$$V_w = \frac{6M_w}{\rho_w} \tag{4}$$

$$V_{MH} = \frac{M_{MH}}{\rho_{MH}} \tag{5}$$

where the density of water (ρ_w) and methane hydrate (ρ_{MH}) are 1 g/cm^3 and 0.918 g/cm^3 [2], ignoring the effect of pressure and temperature; the molar mass of water (M_w) and methane hydrate (M_{MH}) are 18 g/mol and 124.14 g/mol [2], respectively. Thus, 1.25 m^3 of methane hydrate can be formed from 1 m^3 of fresh water.

Therefore the time-lapsed hydrate saturation (S_h) and gas saturation (S_g) could be estimated by Eqs. (6) and (7)

$$S_h = 1.25 \times \frac{(I_0 - I_i) \times S_{w0}}{I_0}, \tag{6}$$

$$S_g = 1 - S_h - S_w, \tag{7}$$

3.1. Temporal characteristics of methane hydrate formation

Case 1 of methane hydrate sample with initial waster saturation S_{w0} = 0.28 was prepared in glass bead BZ-02 to investigate the temporal and spatial characteristic of hydrate formation.

Fig. 2a shows the MI variations, pressure histories and methane hydrate saturation growths curves in Case 1 during methane hydrate formation. The chamber pressure and MRI signal decreased as hydrate was forming by consuming the liquid water and CH_4 gas. At initial stage (almost 0 to 290 min), rapid increases in MI and pressure curves were observed, which indicated that massive hydrate forms in pore spaces. Then, variations in all curves gradually slowed down. It took 800–1000 min before observing the stabilization in MI variations and pressure histories which indicating the complete formation of methane hydrate. Additionally, the variations in MI and pressure showed the same trends, but they were not synchronized in time, possibly because only the middle section of the high-pressure MRI chamber could be monitored by the MRI system with a field of view measuring 30 mm × 30 mm. Pressure transducers were at the top and bottom of the high-pressure MRI chamber, there was a time lag between hydrate formation and gas diffusion. Fig. 2b shows the curves of S_w and S_g and

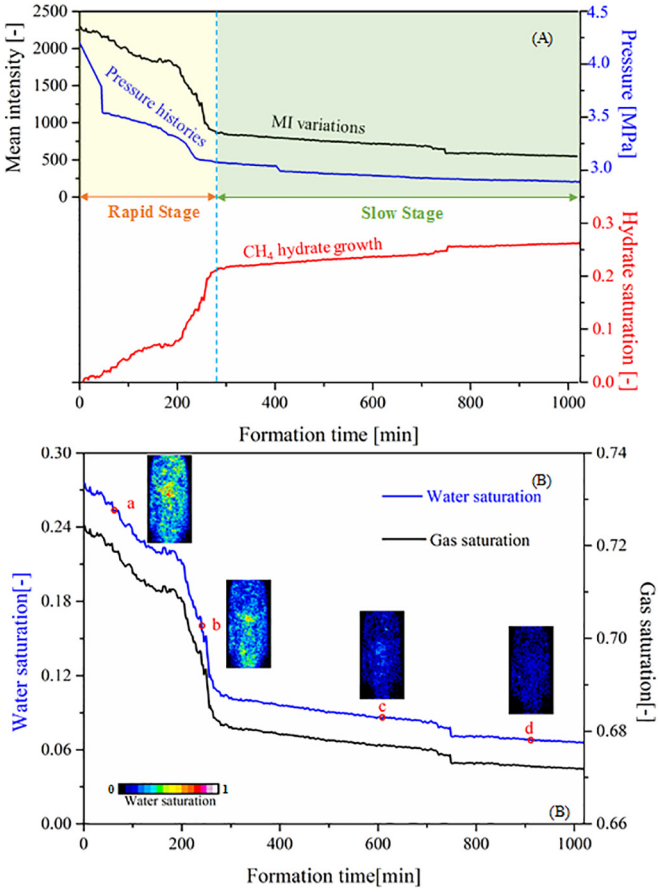

Fig. 2. Methane hydrate formation process in Case 1: (a) Mean intensity (MI) and pressure (P) as a functions of time; (b) S_h and S_g as functions of time.

MRI images obtained during the hydrate formation process in Case 1. The inset MRI images at points "a" and "b" show the stochastic nucleation and growth, which correspond to the stages of gradual and abrupt increase, respectively, during the hydrate formation process. As mentioned above, the value of MI reflects the amount of ^{1}H in the free deionized water distributed in the pores between quartz glass beads; therefore, the darkening of the image indicates a reduction in S_w represented by point "c" in Fig. 2b and an increase in S_h represented by point "d."

Decreased MIs (ΔI) and increased hydrate saturations (ΔS_h) were used to define the consumed rate of liquid water (K_{MI}) and the formation rate of methane hydrate (R_h) in this study, which reflected the variation trend of MI and hydrate saturation curves in Fig. 2a.

$$K_{MI} = \frac{I_i - I_{i+\Delta t}}{\Delta t}, \tag{8}$$

$$R_h = \frac{S_h^{i+\Delta t} - S_h^i}{\Delta t}, \tag{9}$$

where I_i and $I_{i+\Delta t}$ are MI at the "i" and "$i + \Delta t$" minutes, respectively; S_h^i and $S_h^{i+\Delta t}$ are methane hydrate saturation at the "i" and "$i + \Delta t$" minutes, respectively; and Δt is 2 min 8 s, which was the acquisition time resolution of the sequence.

During the whole period of methane hydrate formation, the average formation rate of methane hydrate is defined in Eq. (10).

$$\overline{R_h} = \frac{S_h}{t}, \tag{10}$$

where t is the total time of hydrate dissociation; and S_h is the total methane hydrate saturation that dissociated.

As shown in Fig. 3, in the rapid stage (0–290 min), R_h changes between 2.0×10^{-4} min^{-1} and 8.0×10^{-3} min^{-1}, and the maximum R_h achieves almost 7.7×10^{-3} min^{-1}. During the slow stage (290–1000 min), R_h is almost lower than 5.0×10^{-4} min^{-1}, especially some abnormal moment (such as, $t = 748.8$ min and $R_h = 4.1 \times 10^{-3}$ min^{-1}). These results further demonstrated that methane hydrate formation in porous medium of this study could be divided into two stages: the rapid growth stage ($\overline{R_h} = 7.0 \times 10^{-4}$ min^{-1}) and the followed slow formation stage ($\overline{R_h} = 6.6 \times 10^{-5}$ min^{-1}).

3.2. Dynamic tracking of methane hydrate formation with different initial water saturation

Variations of MRI signals and hydrate saturations predicted and discussed in Section 3.1 have a great use for analyzing the temporal characteristic of methane hydrate formation in porous medium. The

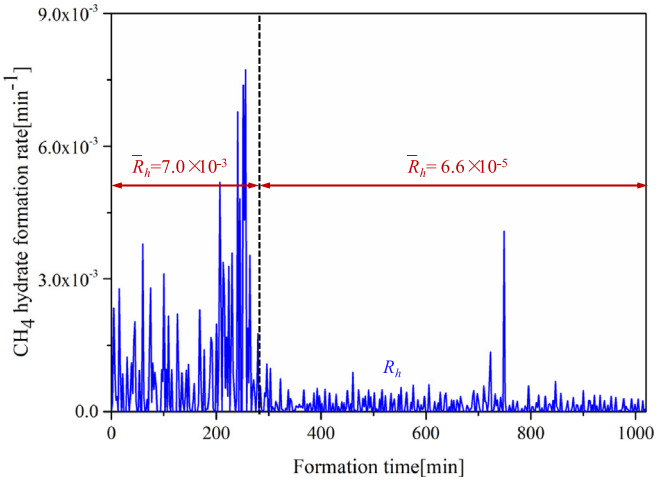

Fig. 3. Methane hydrate formation rate during methane hydrate formation in Case 1.

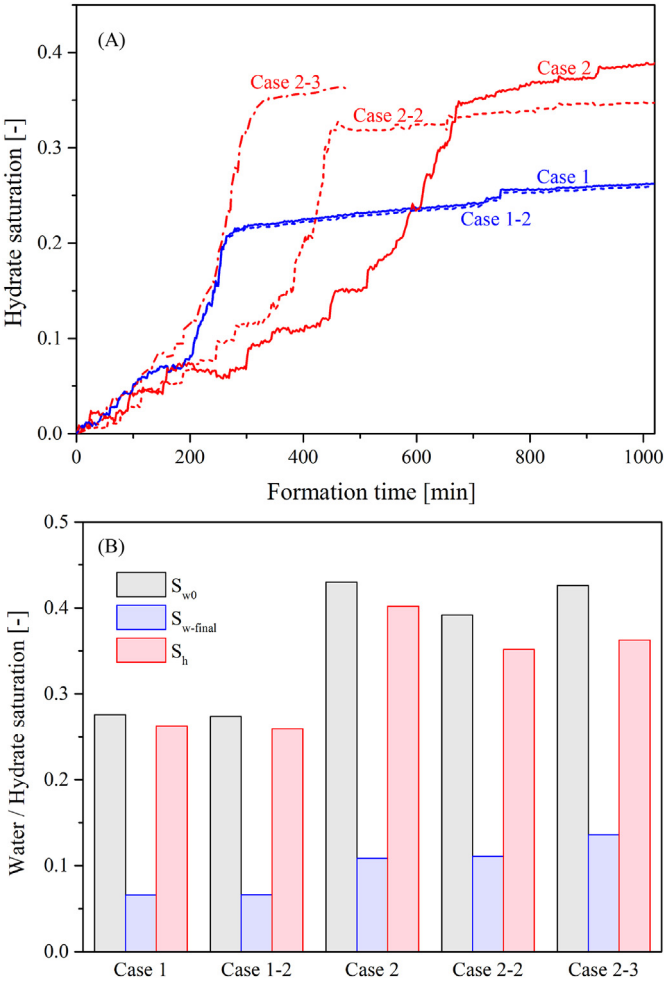

Fig. 4. Methane hydrate formation in Cases 1, 1–2, 2, 2–2 and 2–3.

extension of this result could have important implications for observing methane hydrate growth and formation with different natural conditions. In this study, variously initial water saturations are considered ($S_{w0} = 0.28$ in Case 1 and Case 1–2; $S_{w0} = 0.40$ in Case 2, Case 2–2, and Case 2–3).

Fig. 4a shows the variations of methane hydrate saturations during hydrate formation in porous media with different initial water saturations. The increased hydrate saturation curve in Case 1 and Case 1–2 were similar, which can be explained by that the initial distribution of water and gas were almost the same before methane hydrate formation in these two cases, owing to the repeated porous samples without repacking glass beads and re-injecting water and gas. However, when porous samples mixed with deionized water and CH_4 gas were re-prepared with similar initial water saturation in Cases 2, 2–2, and 2–3, the formation process are quite different, which were contributed to the various distribution of water and gas in pore spaces and the randomness of methane hydrate formation. These results indicated that the growth of crystal hydrate was both affected by the macro-properties (initial water saturation herein) and micro-characteristic (initial water distribution in pore spaces herein). Therefore, the MRI technology would have a great use for analyzing the physical mechanism of hydrate crystal growth by simultaneously obtaining macro- and micro-parameters.

Fig. 4b summarizes the initial water saturation (S_{w0}), the final water saturation ($S_{w\text{-final}}$), and the formed hydrate saturation (S_h) in these five cases. With the increase in S_{w0} from 0.28 to 0.40, S_h raised from 0.26 to 0.40. There results suggested that the increased liquid water could be converted to more methane hydrates when guest gases were abundant

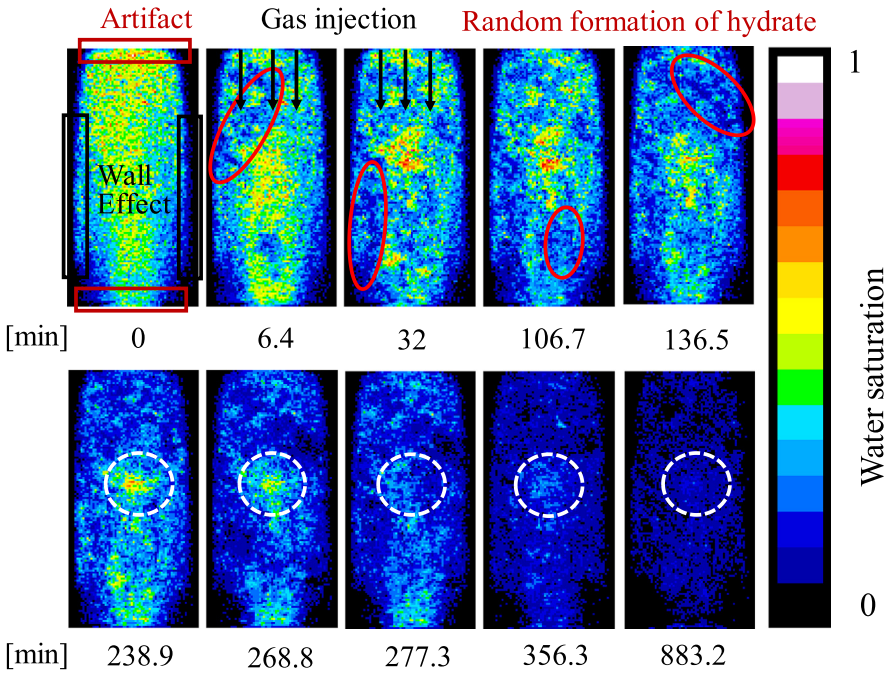

Fig. 5. Water distribution during methane hydrate formation in Case 1.

(high-pressure CH_4 gas in this study). Moreover, $S_{w\text{-final}}$ were small but all were higher than 0.07, which can be explained by that the residual water in pore spaces are trapped within methane hydrate and hard to contact with CH_4 gases to form hydrates.

3.3. Visual analysis of the spatial formation behavior

As mentioned above, only ^1H contained in liquid water could be detected by the experimental MRI system, so the distribution of deionized water during the hydrate formation process could be monitored by detecting ^1H and analyzing the images shown in Fig. 5. The brighter the color, the more water molecules are represented in the image pixel. At the initial time (0 min), the color of the pixels corresponding to the interior wall of the high-pressure MRI chamber was obviously darker than that of pixels corresponding to the middle slice of the sample of porous medium. It can be explained by the "wall effect" [22] and low-pressure CH_4 gas injection before methane hydrate formation. After partial deionized water was discharged during the injection of low-pressure CH_4 gas into the porous medium, more residual water remain in the center of the MRI chamber. Due to the "wall effect", i.e., the porosity near the wall is larger than in the internal space, which means the capillary in the smaller pores near the center has higher capillary force and also has lower intrinsic permeability than the larger pores. Water molecules could not adhere to the smooth inner wall surface, and it had a lower capillary force and higher intrinsic permeability for distribution. Furthermore, the surface of the wall provided a large number of sites for nucleation and heat transfer required for the formation of methane hydrate. Additionally, the top and bottom of the MRI images was affected by an artifact of the MRI device. To observe crystal hydrate formation in porous medium with fast and dynamic MRI monitoring, the spatial resolution was attenuation. In practice, the gradient should be significantly stronger than the internal magnetic field inhomogeneity to ensure that the spatial and temporal precision is essentially sample independent, but it should be weak enough to avoid broadening the lines beyond detection.

Although the high-pressure CH_4 gas was injected from the top of the MRI chamber, with methane hydrate formation in porous medium, the color at the MRI images peripheries first became dark (6.4 min), which suggested that hydrate preferentially growth along the chamber walls due to more efficient heat dissipation. And then the dark area spread to the middle of the imaged section in spatial anisotropy (from 6.4 to 136.5 min), which demonstrated the random formation of crystal hydrate in porous medium (Red elliptical region). Next, the residual liquid water in the white region was slowly converted to the solid hydrate between 238.9 and 356.3 min. It may be caused by that the previous formed hydrate in pore spaces impede the diffusion of CH_4 gas from the top side of the MRI chamber to the surface of residual water in pores. This result further explained the slow formation stage in Fig. 2. Finally, some zones, including the white region, within the MRI chamber were still slightly bright (883.2 min), indicating residually unconverted water in this sample. This may be attributed to water trapped within hydrate shells and not in direct contact with the CH_4 gas to form hydrate.

3.4. Qualitative analysis of hydrate formation behavior in vertical and horizontal sample slices

As previous results, ^1H MRI technology would be a significant method to monitor the chemical conversion process in porous medium involving heat transfer and mass transport. 1D MRI signals and extended 2D and 3D MRI maps could be useful to predicted the quantitative values of local liquid water saturation. In this section, spatially quantified analysis of liquid water in vertical and horizontal sample slices were obtained during methane hydrate formation.

As shown in Fig. 6, MIs in selected vertical slices were different although the decreased trends of these MIs curves were similar, which agreed with the rapid growth stage and the followed slow formation stage in Fig. 2. Such vertical resolved MIs of hydrate formation had shown that the conversion of water into methane hydrate was heterogeneous, suggesting that it was difficult to define the intrinsic growth mechanism in terms of the stochastic conversion processes of hydrates. In slices L and R, the MI approximately matched the whole hydrate sample, whereas in slice M it was higher than the whole MRI images. These results demonstrated that average hydrate formation rates measured for the whole hydrate samples were less insightful to understand the physical mechanism of hydrate growth at micro scale.

As shown in Fig. 7, the different horizontal slices exhibited similar values of MI in the initial stage, which means that water was uniformly

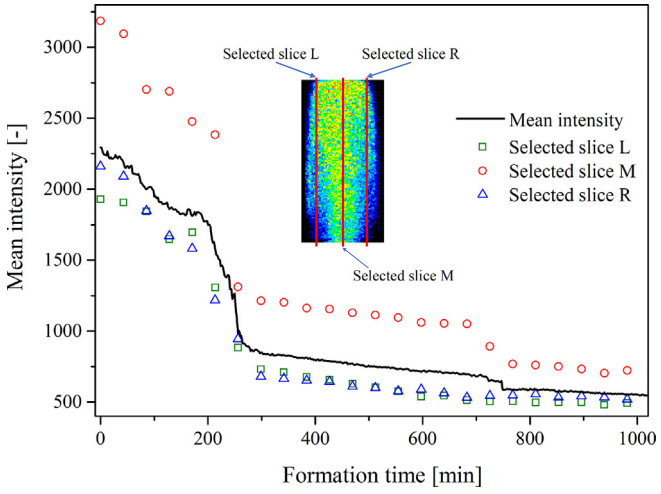

Fig. 6. Water distribution in vertical direction during methane hydrate formation in Case 1.

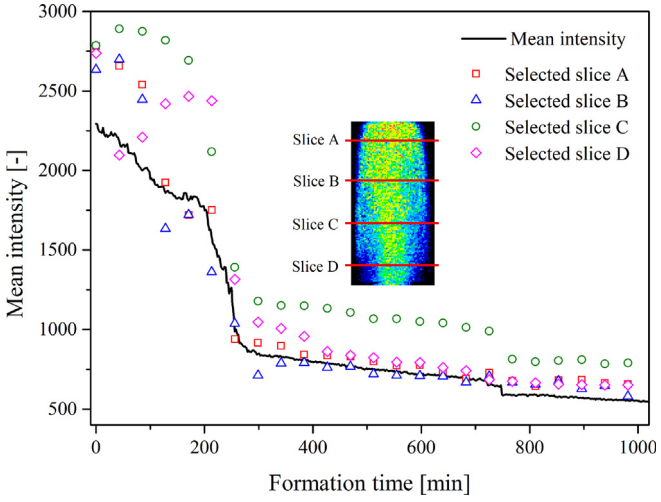

Fig. 7. Water distribution in horizontal direction during methane hydrate formation in Case 1.

distributed in all of them. However, the value of MI of slice A gradually decreased over time, while those of slices B and C first increased and then decreased. The value of MI of slice D decreased in a short initial period, then increased and decreased again. The different trends of MI variations of the four selected slices suggest that water migrated from the top to the bottom of the porous medium sample over time [23]. The initial decrease in MI of slice D implied fast growth of hydrate formation at the bottom during that period, which agrees with the result shown in Fig. 5. As the hydrate blockage broke and the water migration path formed, the water molecules gradually diffused downward, and the value of MI of slice D increased. Finally, the value of MI decreased again as the hydrate formation progressed.

4. Conclusion

The methane hydrate formation process in porous media with different values of initial water saturation was monitored by an MRI system. The spatial and temporal hydrate-formation behavior was measured and analyzed. All curves exhibit a rapid stage and a slow stage; the rapid stage includes a stage of gradual increase (or decrease) and a stage of abrupt increase (or decrease) stage. In terms of hydrate formation in physical space, a blockage in the central region of the sample and a migration path were observed, which demonstrate that water molecules could break through the blockage when driven by high partial pressure and capillary force. Moreover, in the selected vertical slice, water molecules preferred to reside in the middle area all the time because of the "wall effect," and the variation trends in hydrate formation parameters of different slices were similar. However, the distribution of water molecules in different horizontal slices was similar in the initial stage, and different slices exhibited different trends in water distribution during the hydrate formation process, which demonstrated that average hydrate formation rates measured for the whole hydrate samples were less insightful to understand the physical mechanism of hydrate growth at micro scale. These findings are expected to provide guidelines of MRI applications for spatially and temporally analyzing the physical mechanism of hydrate formation and dissociation by simultaneously obtaining macro- and micro-properties.

Acknowledgments

This study was supported by the National Natural Science Foundation of China (Grant No. 51622603) and the Major Program of National Natural Science Foundation of China (Grant No. 51436003).

References

[1] Sloan EJ. Fundamental principles and applications of natural gas hydrates. Nature 2003;426:353–63. https://doi.org/10.1038/nature02135.
[2] Sloan Jr. ED, Koh CA. Clathrate hydrates of natural gases. Boca Raton: CRC Press; 2007.
[3] Ding Y, Xu C, Yu Y, Li X. Methane recovery from natural gas hydrate with simulated IGCC syngas. Energy 2017;120:192–8. https://doi.org/10.1016/j.energy.2016.12.129.
[4] Li X, Xu C, Zhang Y, Ruan X, Li G, Wang Y. Investigation into gas production from natural gas hydrate: a review. Appl Energy 2016;172:286–322. https://doi.org/10.1016/j.apenergy.2016.03.101.
[5] Demirbas A. Methane hydrates as potential energy resource: part 2 – methane production processes from gas hydrates. Energ Conver Manage 2010;51:1562–71. https://doi.org/10.1016/j.enconman.2010.02.014.
[6] Zhao J, Zhang L, Chen X, Zhang Y, Liu Y, Song Y. Combined replacement and depressurization methane hydrate recovery method. Energy Explor Exploit 2016;34:129–39. https://doi.org/10.1177/0144598715623676.
[7] Mahabadi N, Dai S, Seol Y, Jang J. Impact of hydrate saturation on water permeability in hydrate-bearing sediments. J Petrol Sci Eng 2019;174:696–703. https://doi.org/10.1016/j.petrol.2018.11.084.
[8] Kumar A, Maini B, Bishnoi PR, Clarke M, Zatsepina O, Srinivasan S. Experimental determination of permeability in the presence of hydrates and its effect on the dissociation characteristics of gas hydrates in porous media. J Petrol Sci Eng 2010;70:114–22. https://doi.org/10.1016/j.petrol.2009.10.005.
[9] Jang J, Santamarina JC. Hydrate bearing clayey sediments: formation and gas production concepts. Mar Pet Geol 2016;77:235–46. https://doi.org/10.1016/j.marpetgeo.2016.06.013.
[10] Zhang L, Yang L, Wang J, Zhao J, Dong H, Yang M, et al. Enhanced CH_4 recovery and CO_2 storage via thermal stimulation in the CH_4/CO_2 replacement of methane hydrate. Chem Eng J 2017;308:40–9. https://doi.org/10.1016/j.cej.2016.09.047.
[11] Strobel T, Taylor C, Hester K, Dec S, Koh C, Miller K, et al. Molecular hydrogen storage in binary THF-H_2 clathrate hydrates. J Phys Chem B 2006;110(34):17121https://doi.org/10.1021/jp062139n.
[12] Hashemi H, Babaee S, Mohammadi AH, Naidoo P, Ramjugernath D. Experimental measurements and thermodynamic modeling of refrigerant hydrates dissociation conditions. J Chem Thermodyn 2015;80:30–40. https://doi.org/10.1016/j.jct.2014.08.007.
[13] Dong H, Zhang L, Ling Z, Zhao J, Song Y. The controlling factors and ion exclusion mechanism of hydrate-based pollutant removal. ACS Sustain Chem Eng 2019;7:7932–40. https://doi.org/10.1021/acssuschemeng.9b00651.
[14] Tang CC, Miller MC, Cernik RJ, Clark SM, Koh CA, Motie RE, et al. In situ X-ray diffraction method to study natural gas hydrates. Mater Sci Forum 1998;278–281:335–41. https://doi.org/10.4028/www.scientific.net/MSF.278-281.335.
[15] Kida M, Sakagami H, Watanabe M, Jin Y, Takahashi N, Nagao J. Structural properties of methane and butane mixed-gas hydrates. Chem Eng Sci 2016;140:10–5. https://doi.org/10.1016/j.ces.2015.08.047.
[16] Li H, Stanwix P, Aman Z, Johns M, May E, Wang L. Raman spectroscopic studies of clathrate hydrate formation in the presence of hydrophobized particles. J Phys Chem A 2016;120:417–24. https://doi.org/10.1021/acs.jpca.5b11247.
[17] Cheng C, Zhao J, Song Y, Zhu Z, Liu W, Zhang Y, et al. In-situ observation for formation and dissociation of carbon dioxide hydrate in porous media by magnetic resonance imaging. Sci China Earth Sci 2013;56:611–7. https://doi.org/10.1007/s11430-012-4570-5.
[18] Lei L, Liu Z, Seol Y, Boswell R, Dai S. An investigation of hydrate formation in unsaturated sediments using X-ray computed tomography. J Geophys Res Solid Earth 2019;124. https://doi.org/10.1029/2018JB016125.

[19] Zhang L, Zhao J, Dong H, Zhao Y, Liu Y, Zhang Y, et al. Magnetic resonance imaging for in-situ observation of the effect of depressurizing range and rate on methane hydrate dissociation. Chem Eng Sci 2016;144:135–43. https://doi.org/10.1016/j.ces.2016.01.027.

[20] Song Y, Zhang L, Lv Q, Yang M, Ling Z, Zhao J. Assessment of gas production from natural gas hydrate using depressurization, thermal stimulation and combined methods. RSC Adv 2016;6(53):47357https://doi.org/10.1039/C6RA05526E0.

[21] Zhang L, Kuang Y, Zhang X, Song Y, Liu Y, Zhao J. Analyzing the process of gas production from methane hydrate via nitrogen injection. Ind Eng Chem Res 2017;56:7585–92. https://doi.org/10.1021/acs.iecr.7b01011.

[22] Kitagawa A, Denissenko P, Murai Y. Effect of wall surface wettability on collective behavior of hydrogen microbubbles rising along a wall. Exp Thermal Fluid Sci 2017;80:126–38. https://doi.org/10.1016/j.expthermflusci.2016.08.010.

[23] Baldwin BA, Stevens J, Howard JJ, Graue A, Kvamme B, Aspenes E, et al. Using magnetic resonance imaging to monitor CH_4 hydrate formation and spontaneous conversion of CH_4 hydrate to CO_2 hydrate in porous media. Magn Reson Imaging 2009;27:720–6. https://doi.org/10.1016/j.mri.2008.11.011.